Computational Materials Science 155 (2018) 116–128

Contents lists available at ScienceDirect

Computational Materials Science

journal homepage: www.elsevier.com/locate/commatsci

Atomistic simulation study on the shear behavior of Ag/MgO interface

X.Q. Fu[a,c], L.H. Liang[a,c,*], Y.G. Wei[b,*]

[a] LNM, Institute of Mechanics, Chinese Academy of Sciences, Beijing 100190, China
[b] College of Engineering, Peking University, Beijing 100871, China
[c] School of Engineering Science, University of Chinese Academy of Sciences, Beijing 101408, China

ARTICLE INFO

Keywords:
Metal/oxide interface
Interface stress
Interface shear displacement
Misfit dislocation
Atomistic simulation

ABSTRACT

Metal-oxide composites with advanced mechanical properties play an important role in many practical applications, and failure of the metal-oxide interface is directly related to service life of related structures. In order to understand interface failure mechanism, study on atomic-scale separation of metal-oxide interface is significant. In this work, shear behaviors of Ag/MgO (0 0 1) coherent interface and semi-coherent interfaces are studied by employing molecular mechanics method, and some interesting size and defect effects are found. The simulation results show that interface shear stress and displacement appear periodic characteristics with loading. For coherent interface, the interface shear stress and displacement both increase first in each period, then the shear stress drops abruptly after reaching ideal shear strength, and the shear displacement jumps by a unit cell length. The shear strength keeps a constant for all periods. Atomistic simulations of interface systems with different thicknesses show size-independent shear strength and intrinsic interface adhesive energy, but needed loading displacement for the first jump of interface displacement is larger for the thicker systems due to the larger energy consumed by bulk materials. For both 1D and 2D semi-coherent interfaces with dislocations, the shear strength is more than one order of magnitude lower than the ideal shear strength, and the interface displacement changes more continuously with decreased period, which is attributed to different shear mechanism related to dislocation gliding. Comparing 2D semi-coherent interface with 1D case, the shear strength and energy barrier of dislocation motion are both higher due to pinning effect of dislocation intersections.

1. Introduction

In many technological applications, such as thermal barrier coatings (TBCs), catalysts, and composite materials, the mechanical properties of metal/oxide interfaces affect the functionality of the systems [1–4]. In general, interface fracture or slipping under complex loading conditions is the important origin of macroscopic failure. A prominent example is in TBCs, when the residual or loading stress exceeds the critical value, interface crack initiates and crack propagation will eventually lead to the delamination between ceramic top coat and metallic bond layer, which is closely related to micro-scale separation mechanism of the interface. Therefore, it is significant to investigate the failure mechanism of metal/oxide interface at atomistic scale.

Compared with interface tensile fracture, interface shear slipping is more complicated considering the effect of loading condition, interface structure and deformation of the constituent bulk materials. A great deal of experimental [5,6] and theoretical studies [7–9] on the shear behavior of nanoscale metal/ceramic interface systems have been carried out. Through shear and normal compression experiments on CrN/metal-interlayer/Si systems, Zhang et al. revealed that the metal/ceramic chemical interface served to weaken the metal layers near the interface mechanically [5]. Guo et al. found that the shear deformation of Ni/Al_2O_3 interface took place by a successive breaking and re-bonding process of the Al-O bond based on the density function theory (DFT) calculation [8].

Though the development of high resolution transmission electron microscopy (HRTEM) and in-situ instrumented micro/nano scale mechanical testing capabilities make it possible for direct atomic observations as well as quantitative analysis for metal/oxide interfaces [5], it is still quite challenging to study atomic behaviors at and adjacent to the interface during interface dynamics, which hinders the understanding of the physics determining the interface mechanical response. On the simulation side, the availability of accurate metal/oxide interface potentials, which are also convenient for large-scale parallel computing, hampers the molecular dynamics study. The pair potentials extracted from ab-initio adhesive or cohesive energies by Chen-Möbius

* Corresponding authors at: LNM, Institute of Mechanics, Chinese Academy of Sciences, Beijing 100190, China (L. Liang). College of Engineering, Peking University, Beijing 100871, China (Y. Wei).
E-mail addresses: lianglh@lnm.imech.ac.cn (L.H. Liang), weiyg@pku.edu.cn (Y.G. Wei).

https://doi.org/10.1016/j.commatsci.2018.08.047
Received 7 June 2018; Received in revised form 24 August 2018; Accepted 24 August 2018
Available online 29 August 2018
0927-0256/

inversion method [10,11] prove to be a reasonable description of the metal/oxide interfaces [12].

Owning to the simple epitaxial relationships and negligible chemical and charge transfer contribution to bonding, Ag/MgO(0 0 1) system was often chosen as a model of metal/oxide interface [13,14]. Most of the earlier experimental research investigated the structure and morphology of Ag/MgO interface [15–17], and during in-situ growth of Ag on MgO(0 0 1) surfaces, it was observed that the interface structure transformed from coherent to semi-coherent interface, which was characterized by a square misfit dislocation network oriented along ⟨1 1 0⟩ directions [17]. Actually, fundamental properties of these two types of interfaces, such as shear strength and the energy, are key factors determining mechanical response of real Ag/MgO interface.

In this work, shear behaviors of both coherent and semi-coherent Ag/MgO(0 0 1) interfaces are investigated by using atomistic simulation method to shed light on mechanical response of relevant metal/oxide interfaces. First, a coherent interface model and interatomic potentials are introduced in Section 2. The generalized stacking fault energy (GSFE) profile and interplanar stiffness are calculated and analyzed based on the interface potential. These properties are related to mechanical behaviors of Ag/MgO interface systems. Second, a simulation methodology which contains shear loading method and stress calculation method is introduced in Section 3. Next, calculation results of the coherent and semi-coherent interfaces are shown in Section 4 and Section 5, respectively. Interface shear behavior and induced interface compression are studied in Section 4.1. The effect of model thickness is investigated in Section 4.2. The semi-coherent interface structures, computational models and corresponding interface shear behaviors of both one-dimensional (1D) and two-dimensional (2D) dislocation interfaces are presented in Section 5.1 and Section 5.2, respectively. Finally, the conclusion of this paper is given in Section 6.

2. Coherent interface model and interatomic potentials

2.1. Coherent interface model

The computational model of coherent Ag/MgO interface system is shown in Fig. 1(a). Based on experimental observations [18,19], the preferred interface plane is $[0\,0\,1]_{Ag}||[0\,0\,1]_{MgO}$ (z-axis), and the orientation relationship (OR) between Ag and MgO is $[1\,1\,0]_{Ag}||[1\,1\,0]_{MgO}$ (x-axis), $[\bar{1}\,1\,0]_{Ag}||[\bar{1}\,1\,0]_{MgO}$ (y-axis). Note that the Ag/MgO(0 0 1) interface is a fcc/rocksalt structure, and there are three possible interface matching positions: Ag on O site, Ag on Mg site or Ag on hollow site. Ab-initio calculations [11,20] revealed that Ag on O site corresponded to the lowest adhesive energy of Ag/MgO(0 0 1) interface, thus coherent interface of Ag on O site is studied here. The simulation box is periodic in x, y and z directions, and further check indicates that interface area does not affect the simulation results. In z direction, the upper monolayer (ML) and lower ML are fixed boundaries and enough thick vacuum layer is inserted above the upper ML and under the lower ML. The size of the simulation cells are 20 × 10 × L-L, where 20, 10 and L are the number of unit lattices along x, y and z directions, respectively. The thicknesses (L) of Ag and MgO are kept the same and L changes from 5a to 25a to investigate the effect of model thickness.

Fig. 1(b) shows the interfacial atomic configuration, and it can be seen that Ag atoms sit on O sites. The unit cell length along ⟨1 0 0⟩ crystal orientation (z-axis) is lattice constant a (marked by the yellow dashed square). While along ⟨1 1 0⟩ crystal orientations (x- and y-axis), the unit cell length is defined as $1u = \sqrt{2}a/2$ (marked by the red solid square). Since metal is much softer than ceramic, the lattice constants are both taken as that of MgO (4.32 Å) in this coherent model, i.e., the lattices are forced to match at the interface.

2.2. Interatomic potentials and GSFE profile

Pair potentials have been employed to describe the interatomic interactions of Ag/MgO interface systems in our previous work [21], and the interatomic potentials contain both interface potential and bulk potentials. The interface potential is in the Rahman-Stillinger-Lemberg potential (RSL2) form [11,22]:

$$\Phi_{pair}r = D_0 e^{y\left(1-\frac{r}{R_0}\right)} + \frac{a_1}{1+e^{b_1(r-c_1)}} + \frac{a_2}{1+e^{b_2(r-c_2)}} + \frac{a_3}{1+e^{b_3(r-c_3)}} \quad (1)$$

where $\Phi_{pair}r$ is $\Phi_{Ag-O}r$ or $\Phi_{Ag-Mg}r$. The bulk potential $\Phi_{Ag-Ag}r$ is also in the RSL2 form. As an ionic crystal, the oxide-oxide interactions contain both short-range part $\Phi^{SR}(r)$ and long-range coulomb part $\Phi^{Coul}_{Mg-Mg}(r) = \Phi^{Coul}_{O-O}(r) = -\Phi^{Coul}_{Mg-O}(r) = \frac{Q^2_{eff}}{4\pi\,\epsilon_0\,r}$. For Mg—Mg and O—O interactions, the short-range parts $\Phi^{SR}_{Mg-Mg}(r)$ and $\Phi^{SR}_{O-O}(r)$ are in Morse

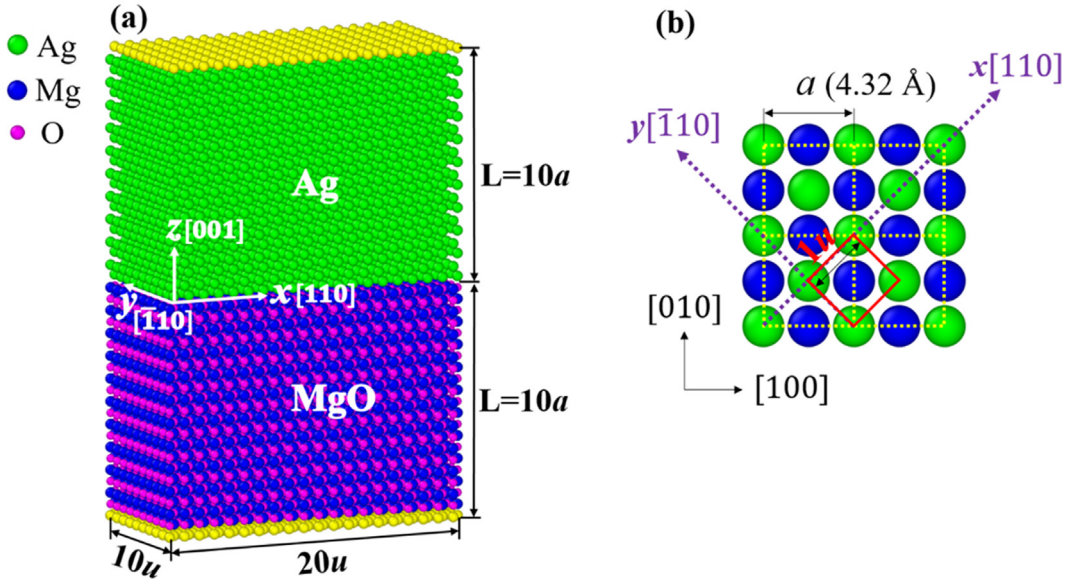

Fig. 1. The computational model of coherent Ag/MgO interface system. (a) Atomic structure of the whole interface model, the top and bottom yellow atoms represent the fixed boundaries. (b) Interfacial atomic configuration showing different unit cells along [1 0 0], [1 1 0] crystal orientations. (For interpretation of the references to colour in this figure legend, the reader is referred to the web version of this article.)

Table 1
Calculated cohesive energy E per unit atom, equilibrium lattice constant a, elastic moduli C_{ij}, and bulk modulus B of Ag and MgO crystals. For comparison, the corresponding experimental and other theoretical results are also listed.

	Ag			MgO		
	This work	Expt.	EAM [23]	This work	Expt.	Long's work [22]
E (eV)	−3.13	−2.96 [24]	−2.85	−18.92	–	−18.94
a (Å)	4.08	4.09 [25], 4.07 [26]	4.09	4.32	4.22 [25]	4.32
C_{11} (GPa)	145.16	122.2 [25] 124 [26]	129.15	318.75	294 [25]	319.2
C_{12} (GPa)	92.13	90.7 [25] 93 [26]	91.09	89.25	93 [25]	89.9
C_{44} (GPa)	92.13	45.4 [25] 46 [26]	56.80	89.17	155 [25]	89.9
B (GPa)	111.62	101 [26]	104.99	82.89	–	–

form $D_0(e^{-y(\frac{r}{R_0}-1)}-2e^{-\frac{y}{2}(\frac{r}{R_0}-1)})$; for Mg—O interaction, the short-range part $\Phi^{SR}_{Mg-O}(r)$ is in the form of $D_0 e^{y(1-\frac{r}{R_0})}$. The detailed explanation and related potential parameters can be found in Table 1 in Ref. [21].

As a basic check for the potentials, some elastic properties and the energy are calculated as listed in Table 1. These theoretical values are compared with other theoretical results, such as Long's work [22] and the results obtained by embedded-atom method (EAM) potential [23], and experimental data [24–26].

The agreement of most parameters indicates that these potentials can reasonably describe the elastic behavior of Ag and MgO. C_{44} is not in good agreement, which is an unavoidable limitation of pair potential approach and $C_{44} = C_{12}$ based on the Cauchy relation [22]. We compared the generalized stacking fault energy (GSFE) of Ag and MgO with those based on the EAM potential [23] and the DFT method [27–31]. Although the absolute values are different more or less, the GSFE forms and the easy shear directions are the same. High estimated shear modulus of Ag will induce its decreased elastic deformation during interface shear process, but it does not affect the interface properties such as interface strength and work of adhesion obviously. In this work, we focus on interface behavior, and the pair potential is good to describe interface properties. For different translation states of Ag/MgO(0 0 1) interface, the adhesive energy curves obtained from the present potential are consistent with the results from ab initio calculation [11]. In short, these potentials prove to be applicable for investigating the slipping process of Ag/MgO interface.

In order to investigate the energy barrier of interface shear, the generalized stacking fault energy (GSFE) of Ag/MgO(0 0 1) interface is calculated by rigidly displacing Ag slab in the [1 0 0] and [0 1 0] directions, and the potential energy after relaxation at each relative position is recorded. Atoms are only allowed to relax in the direction perpendicular to the interface and the GSFE of equilibrium structure is taken as a reference. To do a comparison between the interatomic potential result and the DFT result of GSFE, we also calculated the slip energy vs. distance curves by using the conjugate-gradient method of VASP program [32,33] with GGA functional. The pseudopotential is projector augmented-wave (PAW) [33,34], the plane wave cut-off energy is 600 eV, the k-point mesh is $6 \times 6 \times 1$, generated by the Monkhorst-Park scheme [35,36], and the energy convergence tolerances for electronic self-consistency and ionic relaxation are 10^{-8} eV and 10^{-6} eV respectively. Besides, some GSFE points based on DFT adhesive energies [37,38] are plotted in Fig. 2(b), too.

Fig. 2(a) shows the GSFE profile of ideal Ag/MgO interface. Note that the minimum energy corresponds to Ag on O site and the maximum energy corresponds to Ag on Mg site, which is closely related with interfacial atomic interactions. Unlike normal interface separation, interface shear is a successive process accompanied by continuous bond breaking and rebonding. For Ag/MgO interface, the increase of energy corresponds to increasing Ag—O bond length. When external work is large enough to break all Ag—O bonds, interface shear failure occurs. As shear displacement increases further, the Ag—O bonds reform and correspondingly, the energy returns to its minimum value. The profiles of the energy surface along [1 1 0], [1 0 0] and [0 1 0] crystal orientations are shown in Fig. 2(b). It is clear that for interface slipping, the energy barrier along [1 0 0] and [0 1 0] crystal orientations is higher than that along [1 1 0] crystal orientation. It can be inferred that for ideal Ag/MgO interface, [1 1 0] crystal orientation is easy slip direction. Therefore, in this work the shear direction is along the [1 1 0] crystal orientation (x-axis). Besides, the period of GSFE along [1 1 0] is $|a/2[1\,1\,0]|$, which corresponds to the period of shear traction-displacement curve in the following Section 4.1. From the comparison with the DFT results, the shape of the DFT curves are similar to the results of pair potentials, though there is a larger difference in energy barrier along [1 1 0] crystallographic orientation, which is caused by different first principle methods. Compared with earlier DFT adhesive energy results [37], the barrier height along [1 1 0] is basically the same. We also compared our GSFE profiles of Ag/MgO interface with the fitted two-dimensional Fourier series result [39], the forms and energy barriers are close, too. This proves the present pair potentials can describe the general features of bonding across Ag/MgO interface effectively.

On the other hand, the energy barrier for interface tensile fracture can also be obtained by rigidly displacing Ag slab in z ([0 0 1]) direction and recording the potential energy after relaxation. Then interface tensile cohesive traction and shear cohesive traction are calculated by taking the first order derivative of energy versus displacement. Table 2 lists the energy barriers of interface shear and tensile failures, the cohesive strengths T^{max}_{rigid} in rigid shear/tension, and the corresponding stiffnesses C. The interplanar stiffness is defined as the proportional coefficient of the linear segment in cohesive traction curves [40].

First, the ideal shear strength along [1 0 0] crystal orientation is higher than that along [1 1 0] crystal orientation, which is due to the difference in energy profiles as shown in Fig. 2(b). Second, the tensile stiffness (44.72 GPa/Å) is nearly five times of the shear stiffness (9.38 GPa/Å), which indicates that initial shear of equilibrium Ag/MgO system is more energetically preferred, though the total energy consumed before interface tensile and shear failures are comparable with each other. Besides, owing to the large tensile stiffness, minute interface normal displacement will give rise to a relatively large interface normal stress. Therefore, when analyzing the shear mechanism of coherent Ag/MgO interface, the induced interface normal stress cannot be ignored as discussed in Section 4.1. Note that interface adhesive energy obtained by interface tension here is 0.99 J/m^2, which is roughly in agreement with the DFT calculation results of 0.95 J/m^2 [38], 1.04 J/m^2 [41], and 1.05 J/m^2 [42], etc. [43,44].

3. Simulation methodology

3.1. Shear loading

The computational model described in Section 2.1 is first relaxed

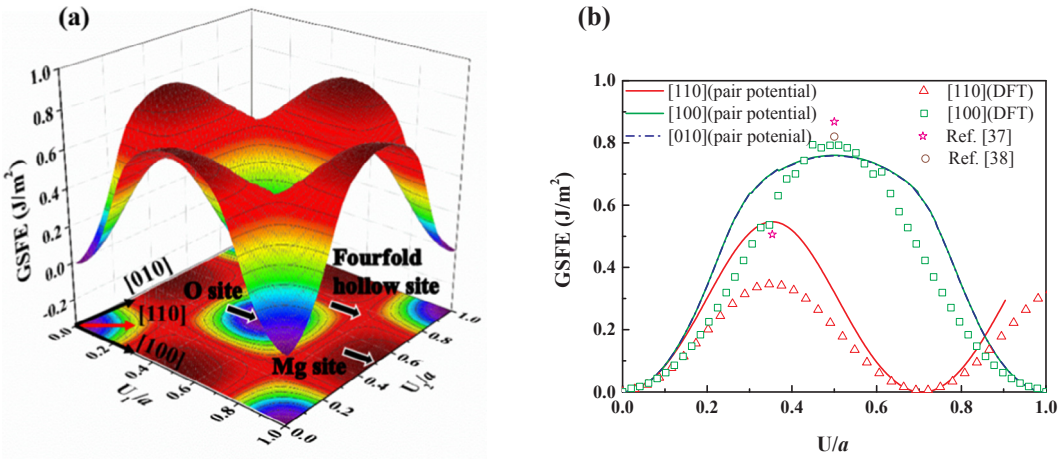

Fig. 2. (a) The GSFE surface of coherent Ag/MgO interface. (b) The profiles of the GSFE along [1 1 0], [1 0 0] and [0 1 0] crystal orientations (lines). DFT results as a comparison (symbols). Distance denotes the relative position of Ag to MgO during interface shear.

Table 2
The energy barriers ΔU_{coh} of interface shear and tensile failure, the cohesive strengths T_{rigid}^{max} in rigid shear/tension, and the corresponding stiffness C.

		ΔU_{coh} (J/m^2)	T_{rigid}^{max} (GPa)	C (GPa/Å)
Shear	[1 1 0]	0.55	5.76	9.38
	[1 0 0]	0.76	8.25	9.38
Tension	[0 0 1]	0.99	8.85	44.72

through two molecular static methods-the FIRE algorithm and the conjugate gradient (CG) algorithm with a force convergence tolerance of 0.01 pN. Since Ag is stretched to match MgO lattice in the coherent interface model, Ag film is subjected to relatively large transverse stress. Then we conduct static simulations at 0 K. As shown in Fig. 3, the upper and lower MLs marked by the black boxes are totally fixed, i.e., the boundary atoms are not allowed to move in the direction perpendicular to the interface. Displacement controlled shear loading along x direction is quasi-statically applied to the fixed Ag ML with a small step size of 0.01Å. Further test indicates that 0.01 Å is small enough to capture the breaking and rebonding of Ag-O bond. In order to improve the computational speed for large coherent models, the step size of displacement is 0.05 Å in the initial loading stage and reset to 0.01 Å when shear traction is close to its critical value. The mobile atoms are relaxed under interatomic potentials at each loading displacement D.

The equilibrium interface spacing $\Delta_0 = 2.39$Å, and interface spacing during loading is Δ. Atom displacements d_t are relative to their initial positions in the relaxed interface structure and averaged in each atomic layer. Interface tangential displacement $\delta_t = d_{t0}(\text{Ag}) - d_{t0}(\text{MgO})$ and normal displacement $\delta_n = \Delta - \Delta_0$ are the relative displacements between Ag ML and MgO ML adjacent to the interface. The subscript t and n represent shear and tensile directions, respectively. σ denotes general stress and T represents the stress at interface. We use the LAMMPS code [45] for atomistic simulations and Ovito [46] software to visualize atomic structures. Standard Ewald summation [47] is performed to compute long-range Coulomb interactions. Considering the diversity of stress calculation methods in atomistic simulations, next we discuss the calculation of interface stress in detail.

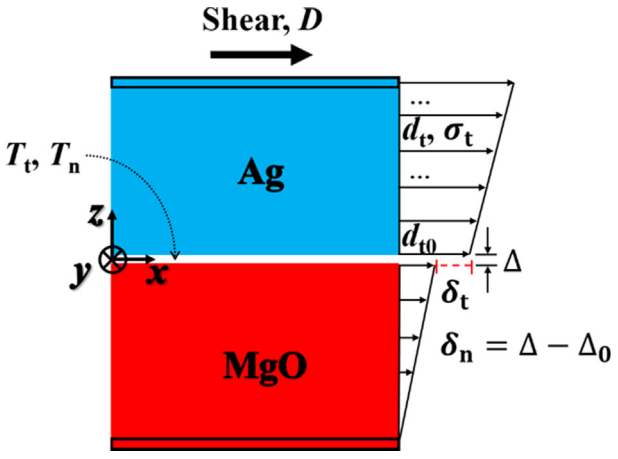

Fig. 3. Schematic illustration of the displacement controlled shear loading applied on the Ag/MgO interface system.

3.2. Interface stress calculation

In this work, four methods to calculate interface stress are considered:

(1) Virial stress (σ^I)

The concept of Virial stress was introduced by Irving Kirkwood [48] in deriving the equations of hydrodynamics in 1950. Its basic expression is as follows:

$$\sigma_{\alpha\beta} = \frac{1}{\Omega}\sum_{i=1}^{N}\left(-m^{(i)}(u_\alpha^{(i)}-\overline{u}_\alpha)(u_\beta^{(i)}-\overline{u}_\beta) + \frac{1}{2}\sum_{j\neq i}(x_\alpha^{(j)}-x_\alpha^{(i)})f_\beta^{(ij)}\right) \quad (2)$$

where $\sigma_{\alpha\beta}$ denotes the average stress in the selected volume Ω, α and β denote the direction of stress. $m^{(i)}$ denotes the mass of the ith atom in volume Ω, $u^{(i)}$ and $x^{(i)}$ are the velocity and position of the ith atom, respectively, $\overline{u}$ is the average velocity of the system, $f^{(ij)}$ denotes the force of atom j on atom i, N is the number of atoms in volume Ω. There is no velocity term in our molecular statics simulations and all atoms are considered in the calculation.

(2) Metal-ceramic interaction force divided by the interface area (σ^{II})

$$\sigma_{\alpha\beta} = \frac{1}{S}\sum_i\sum_j f_{\alpha\beta}^{(ij)} \quad (3)$$

where $\sigma_{\alpha\beta}$ denotes the stress at interface, α and β denote the direction of stress. $f_{\alpha\beta}^{ij}$ is the interaction force between atom i and atom j through the interface. i and j represent the interacting metal atom and oxide atom near the interface. S is the interface area.

(3) Unit area force exerted on the boundary (σ^{III})

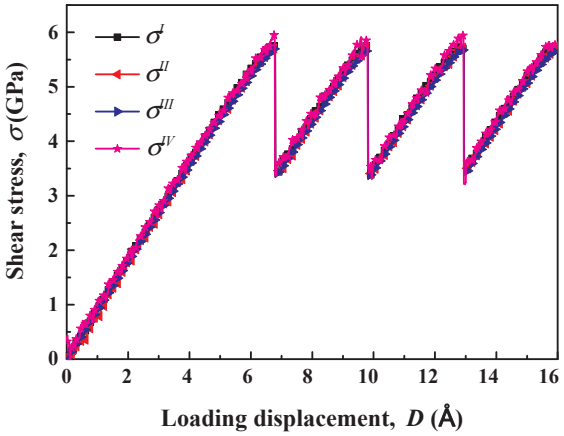

Fig. 4. Comparison of the four calculation methods of interface stress.

$$\sigma = \frac{\sum_{i=1}^{n} f_i}{S'} \tag{4}$$

where f_i denotes the force on the ith atom in the boundary layer, S' denotes the boundary area. In this work, $S' = S$.

(4) Derivative of total energy to the loading displacement (σ^{IV})

$$\sigma = \frac{\mathrm{d}E_{total}}{S\mathrm{d}D} \tag{5}$$

where E_{total} denotes the total energy during interface shear, D is the loading displacement, and S is the interface area.

Taking the coherent 20 × 10 × 10-10 Ag/MgO interface model as an example, and using the simulation method described in Section 3.1, the shear stresses obtained from the above four methods are shown in Fig. 4. It shows that the interface shear stresses calculated by different methods are basically the same. Actually, during the quasi-static loading process the interface system maintains force equilibrium, thus the above four definitions of interface stress are equivalent. In the following part, we choose definition σ^I to calculate the interface traction stress (T_t, T_n).

4. Results of ideal Ag/MgO interface

4.1. Interface shear

The shear process of a coherent Ag/MgO interface system with the model size of 20 × 10 × 10-10 is demonstrated in Fig. 5. It is clear in Fig. 5(a) that the interface displacement changes periodically with increasing loading displacement. The initial small increase of interface displacement is followed by a significant displacement jump, and in every period the change of interface shear displacement is the length of one unit cell length, $\left|\frac{a}{2}[1\,1\,0]\right|$. Note that the shear loading displacement in the first period is greater than in the subsequent periods, so the first period stores more energy.

In Fig. 5(b), the interface shear traction-separation curve is also periodic, the shear stress increases with increasing interface displacement up to the strength value, then drops abruptly to a lower stress level and increases again in the next period. The maximum shear stress (i.e., shear strength) is a constant for all periods, and the period displacement equals $\left|\frac{a}{2}[1\,1\,0]\right|$ as mentioned above. As shear loading displacement increases, more energy is stored in the interface system and interfacial atomic structure deviates from its lowest energy state (Ag atoms on O site) as shown in Fig. 5(c). When external work is sufficient to overcome the energy barrier of all Ag-O bonds breaking, energy burst happens, accompanied by interfacial displacement jump and shear traction drop. The area under loading segment represents the work done for interface shear as shown Fig. 5(b). In the first period, the work W_{coh1} is 0.30 J/m^2, and in subsequent periods, the average work is 0.25 J/m^2. The shear strength of coherent interface (5.75 GPa) is consistent with the result of rigid shear listed in Table 2.

Fig. 5(c) shows the atomic structures corresponding to four critical states (marked by A, B, C, and D in Fig. 5(a) and (b)) from two different perspectives. It demonstrates that in the loading process (A to B), interface slipping and shear deformation of bulk materials occur at the same time. After interface jumps by $\left|\frac{a}{2}[1\,1\,0]\right|$, there is obvious residual elastic deformation in Ag and MgO as shown in map C of Fig. 5(c), and Ag atoms do not sit exactly on O sites when the second period begins.

In order to understand interface shear behavior in detail, the distributions of shear displacements and shear stresses in the whole interface structure under different loading displacements (D) are shown in Fig. 6. Here Z is the average z-coordinates of different atomic layers.

For the shear displacement distribution showed in Fig. 6(a), d_t changes linearly in both Ag (Z > 0) and MgO (Z < 0), and the slope increases with the increase of loading displacement D before interface shear failure (D < 6.80 Å), which indicates greater interplanar shear deformation. Note that D = 6.79 Å and D = 6.80 Å corresponds to points B and C in Fig. 5, respectively. The interplanar slip at the interface (Z = 0) is the biggest for all loading displacements, which can be explained by the obvious discrepancy in interplanar shear stiffness between the interface and bulk materials. When loading displacement reaches a critical value of D = 6.80 Å, interface jumps abruptly, and the slip distance between the two atomic layers adjacent to the interface is one unit cell length. At the same time, part of the stored elastic energy in bulk materials is released, as indicated by the decreased slope of d_t.

Different from the shear displacement distribution, shear stresses σ_t in Ag and MgO are the same and both increase with the increasing loading displacement as shown in Fig. 6(b). Obviously, shear stresses fluctuate in the vicinity of the interface and as D increases, this fluctuation effect becomes more pronounced. This local effect is fundamentally caused by the existence of the interface. After interface jumps, shear stress decreases (see from D = 6.79 Å to D = 6.80 Å), agreeing with that showed in Fig. 5(b) (from point B to C).

There are two kinds of shear: constrained shear and unconstrained shear. In constrained shear, the vertical displacement of boundary atoms is constrained, so a transverse compression is induced, while in unconstrained shear, the normal traction is controlled to be zero [49]. Next, the induced interface compression is discussed in detail.

Fig. 7 shows the induced normal traction and normal displacement of the 20 × 10 × 10-10 coherent Ag/MgO interface system. From the normal displacement change in Fig. 7(a), it can be seen that as shear process continues, the interface is periodically compressed, and the maximum compressive displacement is approximately 0.07 Å.

To investigate the constitutive law for induced compression, a typical traction-separation curve is plotted in Fig. 7(b). It is obvious that the compressive stress increases as two interfacial atomic layers approach to each other. After the minimum distance point B, these two layers jump back to the position near their initial equilibrium distance, and the magnitude of normal traction decreases. Although induced normal displacement is very small, the corresponding normal traction is non-negligible and its peak value reaches approximately 1 GPa. What's more, this induced interface compression consumes energy. From Fig. 7(b), that energy is calculated to be about 0.004 J/m^2, almost two orders of magnitude smaller than the energy consumed for interface shear (0.30 J/m^2). If the boundary atoms are allowed to move in z direction, there would be no coupling interface compression as discussed for unconstrained shear. However, interface shear cohesive relationship is not affected by the boundary conditions [49].

4.2. The effect of model thickness

Experimental research [1,50,51] has revealed that the thickness of individual layers has a considerable influence on the mechanical properties of metal/ceramic nanolaminates. In this section, the

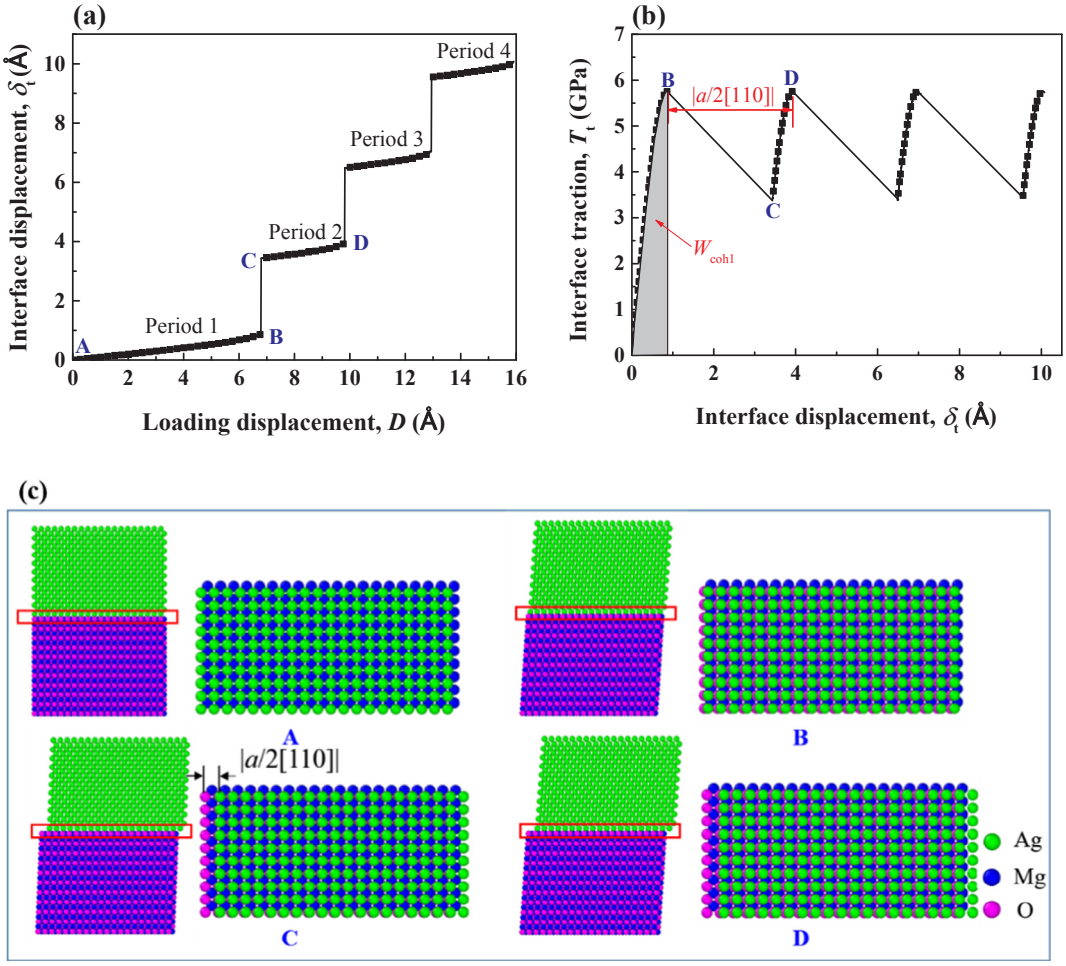

Fig. 5. The shear behavior of 20 × 10 × 10-10 coherent Ag/MgO interface system. (a) Interface displacement jumps as shear loading displacement increases. (b) Interface shear cohesive relationship. (c) Atomic configurations with respect to the marked points A, B, C, and D. For clarity, two maps from different views corresponding to each point are displayed, only two atomic layers adjacent to the interface (marked by the red boxes in left maps) are shown in right maps. (For interpretation of the references to colour in this figure legend, the reader is referred to the web version of this article.)

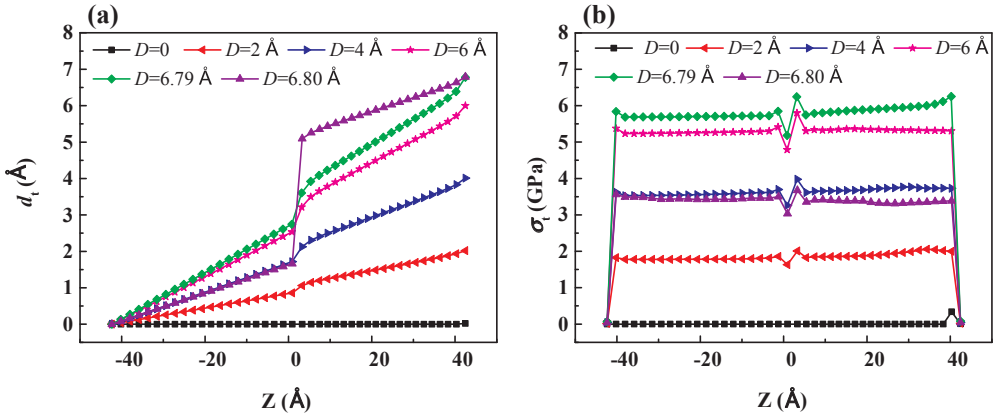

Fig. 6. The distribution of shear displacements and shear stresses in the 20 × 10 × 10-10 coherent Ag/MgO interface system at several loading displacements *D*. (a) Shear displacements at each atomic layer. (b) Shear stresses at each atomic layer. Z = 0: interface; Z < 0: MgO; Z > 0: Ag.

interface traction of coherent Ag/MgO interface systems with different model thicknesses is investigated and the effect of model thickness is analyzed from the point of energy.

Fig. 8 shows the shear traction-separation law of coherent Ag/MgO interface systems with model thickness ranging from 4 nm to 20 nm. Similar to Fig. 5(b), all curves in Fig. 8 contain both linear increased stage and jumping stage in one period. Since model thickness has nearly no effect on the relaxed interface configuration for coherent Ag/MgO interface, the change of shear traction up to the strength in the first period is the same, i.e., the shear strength is thickness-independent. However, thicker interfacial models have larger elastic deformation energy, and interfacial atoms deviate from their equilibrium positions in greater magnitude after interface jump, so the corresponding starting traction (marked by the brown oval) in subsequent period is higher.

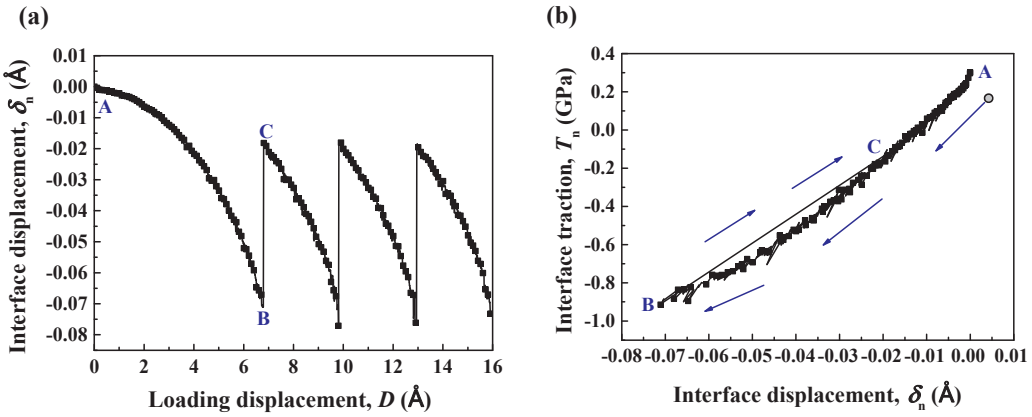

Fig. 7. The coupling interface compression of 20 × 10 × 10-10 coherent Ag/MgO interface system. (a) Interfacial compression displacement increases as loading displacement D increases. (b) Coupling normal stress-displacement relationship.

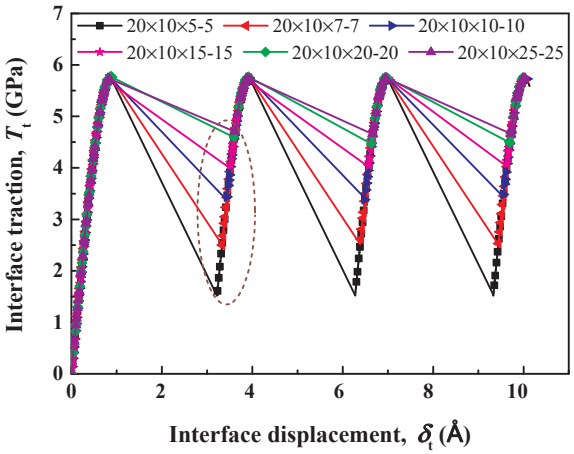

Fig. 8. Shear traction-separation relationship of coherent Ag/MgO interface systems with model thickness ranging from 4 nm to 20 nm.

Fig. 9 shows the change of interface tangential displacements of coherent Ag/MgO interface systems with different model thicknesses. Firstly, the thicker the model is, the larger loading displacement is required for the first interface jump and the greater degree atoms deviate from their equilibrium positions at the beginning of a new shear cycle (marked by the brown arrows). Secondly, from the nearly flat interface displacement curve for 20 × 10 × 25-25 model (marked by the brown

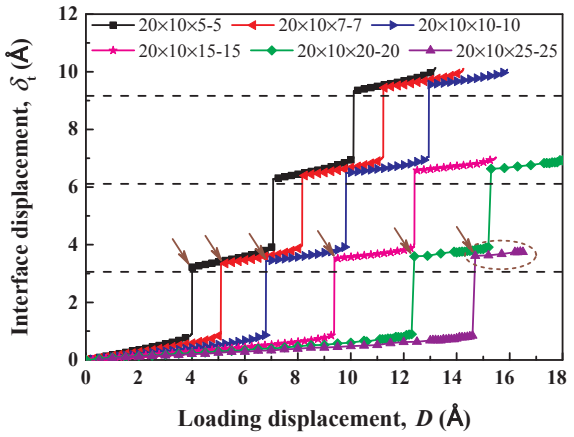

Fig. 9. The change of interface displacement of coherent Ag/MgO interface systems with model thickness ranging from 4 nm to 20 nm.

oval), we can conclude that the interface shear behavior of the larger model is more "brittle", which means there is basically no relative sliding before interface jumps.

Next we analyze the effect of model thickness from the point of energy. In ideal interface systems, there is no plastic deformation during interface shear, so external work transforms into two parts: the energy consumed by the interface W_{coh} and the elastic energy stored in bulk materials E_{bulk}. Since the energies caused by interface compression for different thickness models (0.004–0.006 J/m^2) are very small compared with those consumed for interface shear, only the areas under traction-separation curves in Fig. 8 are used to calculate W_{coh}. The energy stored in bulk materials can be taken as the difference between total energy ΔE and W_{coh} ($E_{bulk} = \Delta E - W_{coh}$). In order to investigate the energy distribution in the interface and bulk materials of different thickness models in interface shear process, the curves of total energy change E are drawn, as shown in Fig. 10. The initial equilibrium structure is taken as a reference in energy calculation.

From Fig. 10(a), it can be seen that interface shear corresponds to regular total energy change. When shear loading displacement increases to the point of interfacial shear jump, the total energy of Ag/MgO interface system increases by ΔE_1. Then the total energy decreases to E', as interfacial atoms return to a lower energy configuration. With further shear loading, the total energy increases by a lower amount, ΔE_2, to the next critical state. So ΔE_1 is the energy barrier of coherent Ag/MgO interface slipping. E' represents the degree of residual deformation in bulk materials and ΔE_2 is the energy required for subsequent interface shear. Table 3 lists the values of ΔE_1, ΔE_2, and the cohesive work of Ag/MgO interface systems with various model thicknesses based on Figs. 10(b) and 8.

By analyzing the data in Table 3, the effect of model thickness on the shear behavior of coherent Ag/MgO interface systems can be learned. In the first period, the energy consumed at the interface when shear failure occurs, W_{coh1}, is almost the same for different models. It reflects the intrinsic interface adhesive properties and is close to the interface fracture energy obtained from previous study [21]. However, ΔE_1 increases proportionally with the increase of model size, as more elastic energy is stored in the thicker models. Obviously, their ratio $W_{coh1}/\Delta E_1$ decreases as model thickness increases. After the first period, W_{coh2} and ΔE_2 are both smaller compared with the values in the first period. ΔE_2 still increases with the increase of model size, while W_{coh2} for the thicker model is smaller. Both values converge to constants and their ratio $W_{coh2}/\Delta E_2$ converges to 0.114. From the above analysis, we can conclude that within a certain range of Ag/MgO model thickness, after initial shear failure, the subsequent interface slipping is easier for the thicker models.

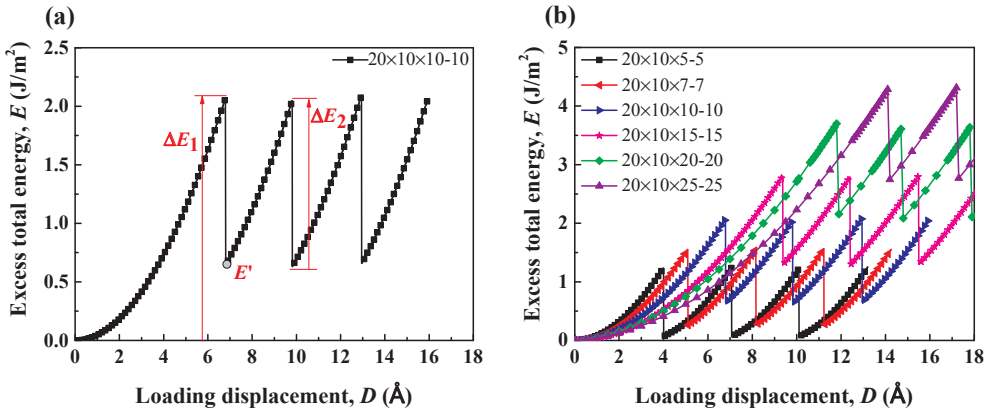

Fig. 10. Total energy change of coherent Ag/MgO interface system with model thickness ranging from 4 nm to 20 nm. (a) Total energy change of 20 × 10 × 10-10 model. ΔE_1: total energy increase in the first period. ΔE_2: total energy increase in the second period. E': stored elastic energy in the system. (b) Total energy change of different thickness models.

Table 3
Some key interface and system energy values during the shear process of Ag/MgO interface models with thickness ranging from 4 nm to 20 nm. W_{coh1} and W_{coh2}: the cohesive work in the first period and the second period based on Fig. 8. ΔE_1 and ΔE_2: the energy barrier in the first period and the second period in Fig. 10(b).

Model size	W_{coh1} (J/m^2)	W_{coh2} (J/m^2)	ΔE_1 (J/m^2)	ΔE_2 (J/m^2)	$W_{coh1}/\Delta E_1$	$W_{coh2}/\Delta E_2$
20 × 10 × 5-5	0.322	0.317	1.23	1.16	0.262	0.273
20 × 10 × 7-7	0.330	0.296	1.55	1.30	0.213	0.228
20 × 10 × 10-10	0.300	0.254	2.07	1.41	0.145	0.180
20 × 10 × 15-15	0.324	0.209	2.80	1.49	0.116	0.140
20 × 10 × 20-20	0.305	0.184	3.63	1.58	0.0840	0.116
20 × 10 × 25-25	0.300	0.175	4.29	1.54	0.0699	0.114

5. Shear behavior of semi-coherent Ag/MgO interface

5.1. Shear behavior of semi-coherent interface with a 1D dislocation

The computational model of Ag/MgO interface with one dislocation is shown in Fig. 11(a). The dislocation with Burgers vector **b** = a/2[1 1 0] is constructed by inserting a layer of Ag atoms along the (1 1 1) plane into the ideal interface structure, and the dislocation line is parallel to the *y* axis, with the dislocation edge in the first metal ML. Fig. 11(b) shows the interfacial atomic configuration. Considering the lattice mismatch between Ag and MgO (lattice constant $a_{MgO}/a_{Ag} \approx 20/19$), there are 19 unit MgO cells and 20 unit Ag cells along the x direction. The dislocation spacing is 5.8 nm and the dislocation density ρ is 0.0172 Å^{-1}. Then the model is subjected to the same relaxation and shear loading as described in Section 3. Simulation results are as follows.

The shear mechanism of semi-coherent Ag/MgO interface with a 1D dislocation is completely different from that of coherent interface. As shown in Fig. 12, the gliding motion of the dislocation, rather than bond breaking, leads to interface shear. Unlike Fig. 5(a), in Fig. 12(a) the interface shear displacement increases almost in the same degree with loading displacement, with much smaller period and relatively unobvious jumps, so the shear deformation of semi-coherent interface is more continuous. Besides, the elastic deformation in bulk materials is small and external work is consumed mainly by interface shear. When Ag slab slips by the length of one Burger's vector $|\mathbf{b}| = \left|\frac{a}{2}[1\,1\,0]\right|$ relative to MgO slab, the dislocation slides across the entire interface, with 19 interface displacement jumps as shown in Fig. 12(c).

Fig. 12(b) shows the shear strength of semi-coherent Ag/MgO interface fluctuates and the average shear strength is 0.126 GPa, more than one order of magnitude lower than that of coherent Ag/MgO interface (5.75 GPa). In every period, when the dislocation jumps to the

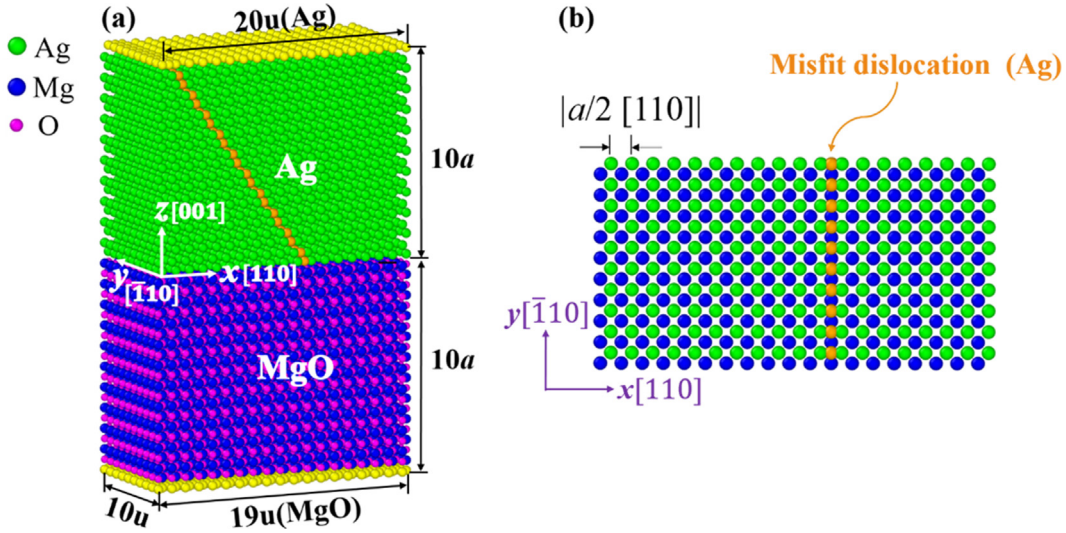

Fig. 11. The computational model of 1D dislocation Ag/MgO interface system. (a) Semi-coherent interface model with one dislocation by inserting an extra Ag layer along the (1 1 1) plane into the ideal interface structure. (b) Interfacial atomic configuration which shows the position of dislocation before relaxation.

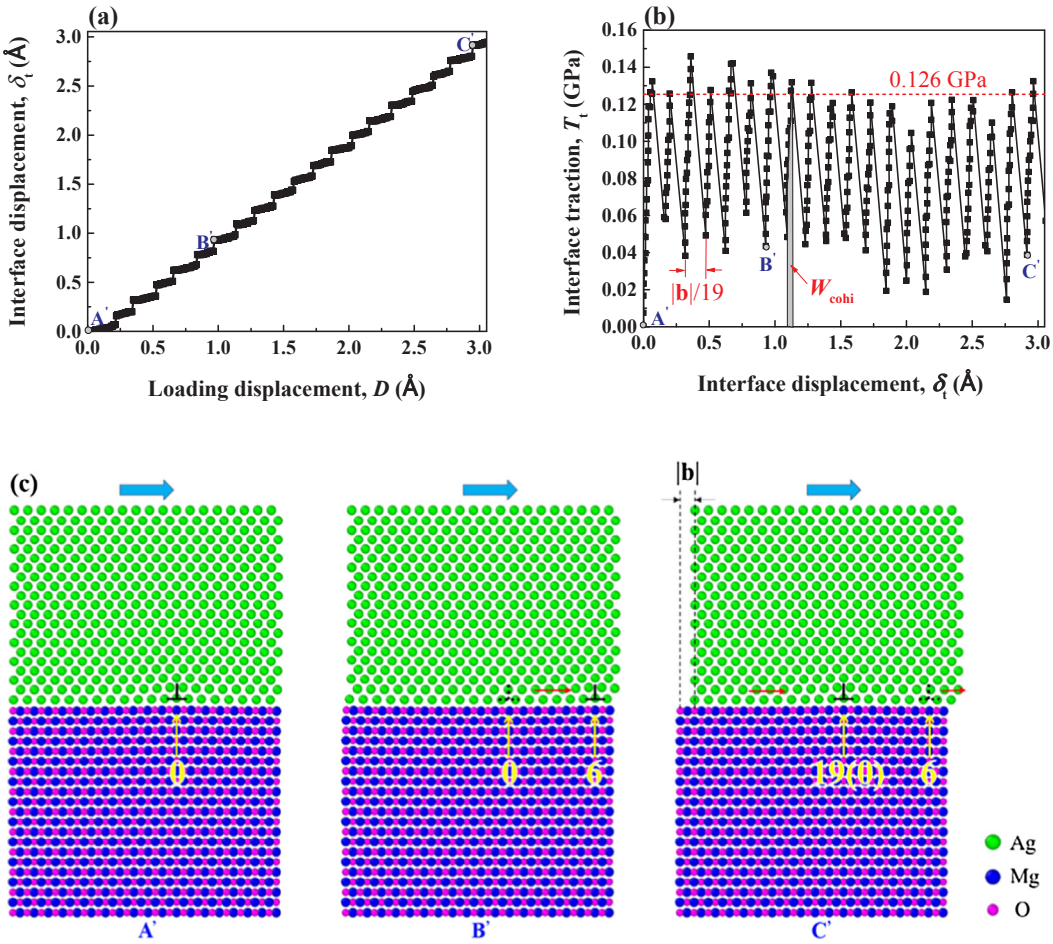

Fig. 12. Interface shear behavior of semi-coherent Ag/MgO interface system with a 1D dislocation. (a) Interface displacement increases with the motion of the dislocation. (b) Interface shear traction-separation relationship. (c) Atomic configurations with respect to the marked points A′, B′, and C′ in (a) and (b). The locations of the dislocation during interface shear are marked.

next position, interface traction drops and the period of the traction-displacement curve is $|\mathbf{b}|/19$. The atomic configurations corresponding to points A', B' and C' on the traction curve are shown in Fig. 12(c). Here "0" represents the initial position of the dislocation, "6" and "19" represent the times of dislocation movements. When the dislocation returns to its initial position, the interface slips by the length of $|\mathbf{b}|$. It also shows that Ag atoms sit on Mg sites in dislocation core area and on O sites in the region between the dislocation lines (DLs). At the same time, the interface is the slip plane of the dislocation.

5.2. Shear behavior of semi-coherent interface with 2D misfit dislocations

In order to understand the shear mechanism of semi-coherent interface further, an interface model with 2D misfit dislocations is built as shown in Fig. 13. There are 19 MgO unit cells and 20 Ag unit cells along both directions parallel to the interface (x [1 1 0] and y[$\bar{1}$ 1 0]), and the thickness is the same with that in the model with 1D dislocation. Interface atomic configuration before relaxation is shown in Fig. 13(b), three zones with Ag on O site, Ag on Mg site and transition zones (bridge site and hollow site) can be seen. After the relaxation of interface structure, mutually perpendicular dislocation lines (marked by the dashed black lines) and dislocation intersections (marked by the stars, i.e., Mg site) are clearer as shown in Fig. 14. The dislocation spacing is still 5.8 nm.

Fig. 14 shows the plot of disregistry vector at the interface. The interface area of 2D model is shown by the blue square. It can be seen that the dislocation lines along ⟨1 1 0⟩ and ⟨$\bar{1}$ 1 0⟩ constitute misfit dislocation network. The dislocations are edge type with Burgers vector $\mathbf{b} = \frac{a_{Ag}}{2}\langle 1\,1\,0\rangle$, which is consistent with experimental observations by HRTEM and grazing x-ray diffraction [15,17]. Comparing this relaxed structure with initial structure in Fig. 13(b), it can be found that O site regions with lower energy extend while Mg site regions shrink at the dislocation intersections (nodes). Along dislocation lines Ag atoms transform between Mg site and hollow site; bridge site is near the nodes. Note that high energy sites (hollow site, bridge site and Mg site) are all along or near the misfit dislocation lines, so one can infer that under shear loading, atoms at these regions will move first. The model is subjected to the same shear loading as described in Section 3. Simulation results are as follows.

For 2D semi-coherent interface with misfit dislocation networks, the shear mechanism is slightly different from that of 1D semi-coherent interface, due to the existence of dislocation nodes. In Fig. 15(a) the interface displacement still increases almost linearly with the increase of loading displacement, whereas, the jump distance of dislocation is two times larger. In Fig. 15(b), owing to the pinning effect of dislocation nodes, interface shear strength (0.415 GPa) is higher than that of 1D semi-coherent interface (0.126 GPa), but still much lower than the ideal shear strength (5.75 GPa). Besides, the period $\frac{|\vec{\mathbf{b}}|}{9.5}$ corresponds to the motion of dislocation network. Fig. 15(c) shows the interface atomic configurations at some critical points on the traction-displacement curve and the red arrows mark the positions of misfit dislocation during interface shear. It shows that interface shear is caused by the gliding motion of misfit dislocation network, which is mainly reflected by the motion of dislocation nodes.

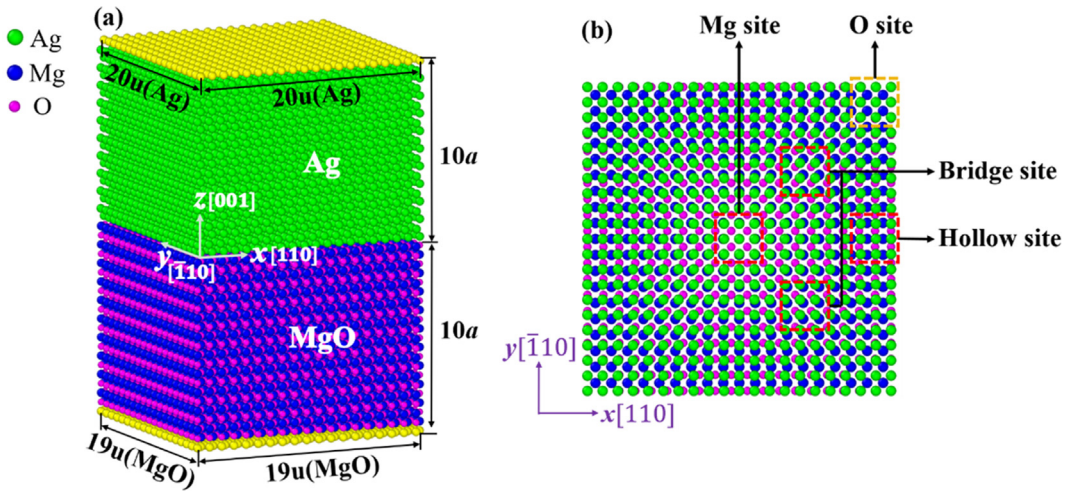

Fig. 13. (a) Semi-coherent interface model with 2D misfit dislocation network. (b) Interfacial atomic configuration before relaxation.

In Section 4.1, the induced interface compression is studied in detail. For semi-coherent Ag/MgO interface (1D and 2D), the induced normal stress is very small, which changes within 1 MPa, and the interface normal distance is basically unchanged. In short, misfit dislocation can not only reduce the shear strength dramatically, but also eliminate the coupling effect between interface shear and compression.

5.3. Energy comparison between 1D and 2D semi-coherent interfaces

In 1D and 2D semi-coherent interfaces, dislocation motion causes a change in total energy. As shown in Fig. 16, total energy E increases in the initial stage of dislocation motion. When E reaches the critical value, misfit dislocation jumps to the next stable position and part of the energy is released. Therefore, ΔE_i represents the energy barrier of dislocation motion. Due to the effect of dislocation intersections, the energy barrier ΔE_i of 2D semi-coherent interface ($\approx 0.010\ J/m^2$) is higher than that of 1D semi-coherent interface ($\approx 0.0014\ J/m^2$).

Similar to the energy analysis for coherent interface in Section 4.2, the cohesive work $W_{coh} = \sum_{i=1}^{i=n} W_{cohi}$ (n = 9.5 or 19 for 2D or 1D semi-coherent interface) and energy barrier $\Delta E = \sum_{i=1}^{i=n} \Delta E_i$ when interface slips the length of a Burgers vector, as well as the shear strength T_t^{max} and the period of traction-displacement curve l_p are listed in Table 4. For comparison, the corresponding values of coherent interface are also listed, where the energy values are W_{coh1} and ΔE_1 in Table 3.

From above data, we see that W_{coh} and ΔE of both semi-coherent interfaces are nearly two orders of magnitude lower than the corresponding values of coherent interface, so the existence of misfit dislocation can significantly reduce the energy barrier of interface shear. By analyzing the energy ratio $W_{coh}/\Delta E$, one can estimate the degree of residual deformation in bulk materials. For 1D and 2D semi-coherent interfaces, the ratios are both higher than coherent interface, which indicates less residual deformation in bulk materials.

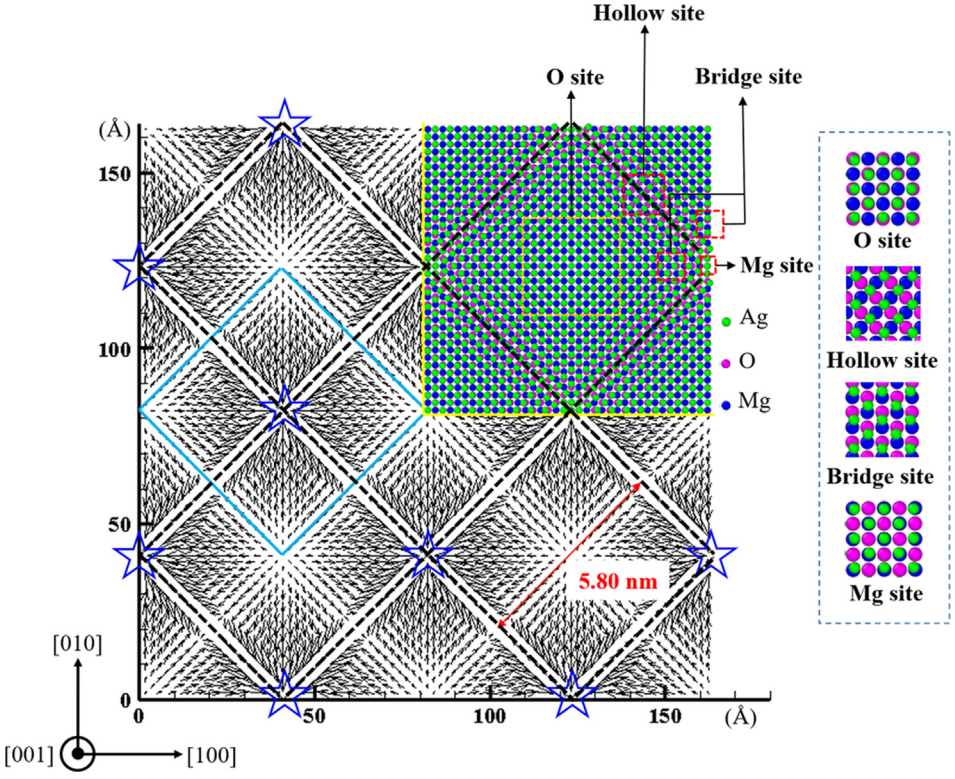

Fig. 14. Disregistry plot of the relaxed Ag/MgO interface with 2D misfit dislocations. Four possible structures are shown. O site or Mg site: Ag atoms are on top of the O atoms or Mg atoms. Hollow site: Ag atoms are at the center of a square outlined by two Mg and two O atoms. Bridge site: Ag atoms are at the middle of the neighboring Mg and O atoms.

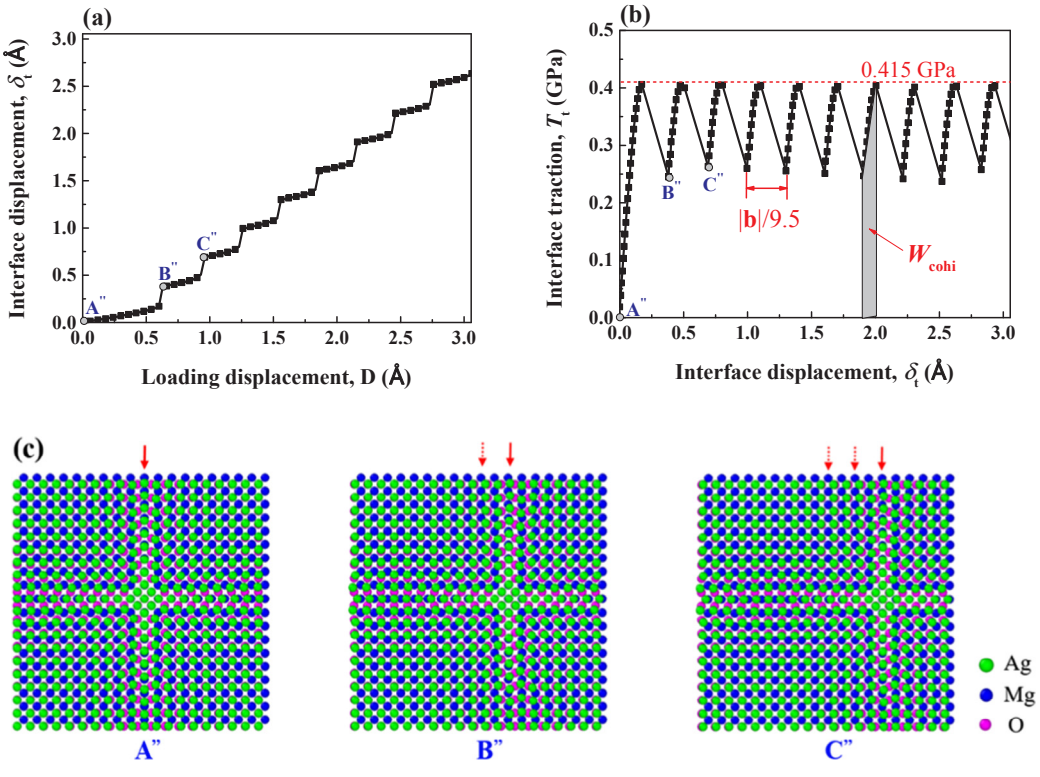

Fig. 15. Interface shear behavior of 2D semi-coherent Ag/MgO interface system. (a) Interface displacement increases with the motion of misfit dislocation. (b) Interface traction-displacement relationship. (c) Interface atomic configurations with respect to the marked points A″, B″, and C″ in (a) and (b). The locations of the misfit dislocation during interface shear are marked.

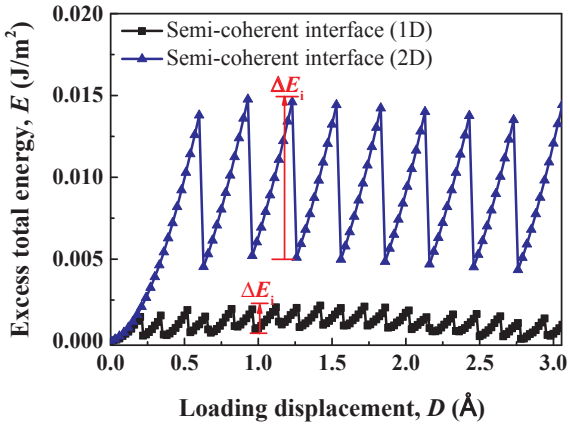

Fig. 16. Total energy change of 1D and 2D semi-coherent Ag/MgO interface systems.

Table 4
Some key values in interface shear process for coherent and semi-coherent Ag/MgO interfaces with thickness of 8.5 nm. W_{coh} and ΔE: cohesive work and energy barrier when interface slips a length of Burgers vector. T_t^{max}: shear strength. l_p: the period of traction-displacement relationship.

	W_{coh} (J/m^2)	ΔE (J/m^2)	$W_{coh}/\Delta E$	T_t^{max} (GPa)	l_p (Å)
Coherent (20 × 10 × 10-10)	0.300	2.07	0.145	5.75	|a/2[1 1 0]| (= |**b**|)
1D Semi-coherent (19 × 10 × 10-10)	0.00821	0.0238	0.346	0.126	|**b**|/19
2D Semi-coherent (19 × 19 × 10-10)	0.0365	0.0972	0.376	0.405	|**b**|/9.5

Compared with coherent interface, the shear strengths of two semi-coherent interfaces are both more than one order of magnitude lower. They are within the range of experimental shear strengths of metal/ceramic interfaces [5,52,53]. However, since the effects of porosity, grain boundaries and temperature, etc., are not considered, these shear strengths of defect interfaces are higher than many experimental results. Besides, comparing the 2D semi-coherent interface with the 1D semi-coherent interface, the interface shear strength (T_t^{max}) and energy barrier (W_{coh}, ΔE) are both higher, which is due to the pinning effect of dislocation intersections as mentioned previously.

The period of traction-displacement relationship (l_p) for coherent interface is one unit cell length, which equals the length of Burgers vector |**b**|. While for 1D and 2D semi-coherent interfaces, the periods are much shorter, with |**b**|/19 for 1D case and |**b**|/9.5 for 2D case. In fact, l_p is closely related with interface structure and dislocation motion. In addition, shorter periods give rise to more continuous interface sliding.

6. Conclusion

In summary, atomistic simulations of both coherent and semi-coherent Ag/MgO interface systems are conducted to investigate their shear mechanism, the effects of model thickness and misfit dislocation.

Coherent interface shears in a “jump” manner, with the jump distance equals the length of unit cell along the shear direction, and the ideal shear strength is 5.75 GPa. Besides, the interface relative slip is accompanied with periodically interface compression, and the compressive stress (≈ 1 GPa) is comparable to the ideal shear strength, though the interface normal displacement is quite small.

The distribution of shear displacement reveals that the displacement in Ag and MgO are linearly distributed normal to the interface, with the most obvious relative slip at the interface. The shear stress remains unchanged in the bulk materials and it fluctuates in the vicinity of the interface. As loading displacement increases, this fluctuation becomes more pronounced. In short, in thin films containing a soft metal and a hard ceramic, interface will cause local effect of displacement and stress.

For the effect of model thickness, the thicker models appear to be more “brittle” in the process of interface shear, which means that the

slip distance before the interface jump is negligible. What's more, model thickness does not influence the energy consumed at the interface when interface shear failure occurs. In the following shear process, the thicker model consumes less energy at the interface due to the more elastic energy stored in bulk materials. Nevertheless, the intrinsic interface properties, e.g., interface strength and interface adhesive energy are the same.

The slip process of semi-coherent interface is characterized by the gliding motion of misfit dislocation along the interface. Compared with coherent interface, semi-coherent interface is easier to shear, indicated by the significantly lower values of energy barrier, cohesive work and shear strength. The change of interface shear displacement is relatively continuous. Besides, owing to the existence of dislocation intersections, the interface shear strength of 2D semi-coherent interface is higher than that of 1D case.

The location of misfit dislocation has an important effect on interface mechanical properties. In this work only one location of misfit dislocation is studied. For interfaces with misfit dislocations that end one, two and more layers above the interface, their shear behavior will be studied further.

7. CRediT authorship contribution statement

Xueqiong Fu (Ph D student): Data curation, Software, Investigation, Writing – original draft. **Lihong Liang (Supervisor):** Conceptualization, Methodology, Formal analysis, Funding acquisition, Writing – review & editing. **Yueguang Wei (Supervisor):** Conceptualization, Methodology, Funding acquisition.

Data availability

The raw/processed data required to reproduce these findings cannot be shared at this time due to technical or time limitations.

Acknowledgement

This work was supported by the Nature Science Foundation of China (NSFC, No. 11672296, 11372318, 11432014, 11672301, 11521202), and the Strategic Priority Research Program of the Chinese Academy of Sciences (Grant No. XDB22040501).

Appendix A. Supplementary material

Supplementary data associated with this article can be found, in the online version, at https://doi.org/10.1016/j.commatsci.2018.08.047.

References

[1] M. Damadam, S. Shao, G. Ayoub, H.M. Zbib, Recent advances in modeling of interfaces and mechanical behavior of multilayer metallic/ceramic composites, J. Mater. Sci. 53 (2017) 5604–5617.
[2] N. Li, X.Y. Liu, Review: mechanical behavior of metal/ceramic interfaces in nano-layered composites—experiments and modeling, J. Mater. Sci. 53 (2017) 5562–5583.
[3] W. Wunderlich, The atomistic structure of metal/ceramic interfaces is the key issue for developing better properties, Metals 4 (2014) 410–427.
[4] H.G. Steinruck, C. Cao, Y. Tsao, C.J. Takacs, O. Konovalov, J. Vatamanu, O. Borodin, M.F. Toney, The nanoscale structure of the electrolyte-metal oxide interface, Energy Environ. Sci. 11 (2018) 594–602.
[5] X. Zhang, B. Zhang, Y. Mu, S. Shao, C.D. Wick, B.R. Ramachandran, W.J. Meng, Mechanical failure of metal/ceramic interfacial regions under shear loading, Acta Mater. 138 (2017) 224–236.
[6] W.M. Fr, D.H. Yoon, K. Raju, S. Kim, K.S. Song, J.H. Yu, Interfacial microstructure and shear strength of reactive air brazed oxygen transport membrane ceramic-metal alloy joints, Met. Mater. Int. 24 (2018) 157–169.
[7] A. Sazgar, M.R. Movahhedy, M. Mahnama, S. Sohrabpour, A molecular dynamics study of bond strength and interface conditions in the Al/Al_2O_3 metal–ceramic composites, Comp. Mater. Sci. 109 (2015) 200–208.
[8] X. Guo, F. Shang, Shear strength and sliding behavior of Ni/Al_2O_3 interfaces: A first-principle study, J. Mater. Res. 27 (2012) 1237–1244.
[9] S.K. Yadav, R. Ramprasad, J. Wang, A. Misra, X.Y. Liu, First-principles study of Cu/TiN and Al/TiN interfaces: weak versus strong interfaces, Modell. Simul. Mater. Sci. Eng. 22 (2014) 1–11.
[10] N.X. Chen, Modified Mobius inverse formula and its applications in physics, Phys. Rev. Lett. 64 (1990) 1193–1195.
[11] Y. Long, N.X. Chen, W.Q. Zhang, Pair potentials for a metal–ceramic interface by inversion of adhesive energy, J. Phys.: Condens. Mater. 17 (2005) 2045–2058.
[12] Y. Long, N.X. Chen, H.Y. Wang, Theoretical investigations of misfit dislocations in Pd/MgO(001) interfaces, J. Phys.: Condens. Mater. 17 (2005) 6149–6172.
[13] P.W. Palmberg, T.N. Rhodin, C.J. Todd, Epitaxial growth of gold and silver on magnesium oxide cleaved in ultrahigh vacuum, Appl. Phys. Lett. 11 (1967) 33–35.
[14] A. Barbier, G. Renaud, J. Jupille, Evolution of the cluster shape during the growth of Ag on MgO(001), Surf. Sci. 454 (2000) 979–983.
[15] A. Trampert, F. Ernst, C. Flynn, H. Fischmeister, M. Ru, High resolution transmission electron microscopy studies of the Ag/MgO interface, Acta Metall. Mater. 40 (1992) S227–S236.
[16] J.T.M.D. Hosson, B.J. Kooi, Metal/ceramic interfaces: a microscopic analysis, Surf. Interface Anal. 31 (2001) 637–658.
[17] G. Renaud, P. Guenard, A. Barbier, Misfit dislocation network at the Ag/MgO (001) interface: a grazing-incidence x-ray-scattering study, Phys. Rev. B 58 (1998) 7310–7318.
[18] P. Guenard, G. Renaud, B. Villette, Structure, translational state and morphology of the Ag/MgO(001) interface during its formation, Physica B 221 (1996) 205–209.
[19] O. Robach, G. Renaud, A. Barbier, Structure and morphology of the Ag/MgO(001) interface during in situ growth at room temperature, Phys. Rev. B 60 (1999) 5858–5871.
[20] T. Hong, J.R. Smith, D.J. Srolovitz, Metal/ceramic adhesion: a first principles study of MgO/Al and MgO/Ag, J. Adhes. Sci. Technol. 8 (1994) 837–851.
[21] X.M. You, L.H. Liang, Y.G. Wei, The atomistic simulation study of Ag/MgO interface tension fracture, Comp. Mater. Sci. 142 (2018) 277–284.
[22] Y. Long, N.X. Chen, An atomistic simulation and phenomenological approach of misfit dislocation in metal/oxide interfaces, Surf. Sci. 602 (2008) 1122–1130.
[23] S.M. Foiles, M.I. Baskes, M.S. Daw, Embedded-atom-method functions for the fcc metals Cu, Ag, Au, Ni, Pd, Pt, and their alloys, Phys. Rev. B 33 (1986) 7983–7991.
[24] C. Kittel, D.F. Holcomb, Introduction to solid state physics, Am. J. Phys. 35 (1967) 547–548.
[25] M. Levy, H. Bass, R.R. Stern, Handbook of Elastic Properties of Solids, Liquids, and Gases, Academic Press, New York, 2001.
[26] G. Simmons, H. Wang, Singer Crystal Elastic Properties and Calculated Aggregate Properties: a handbook, MIT Press, Cambridge (MA), 1971.
[27] J. Amodeo, P. Carrez, P. Cordier, Modelling the effect of pressure on the critical shear stress of MgO single crystals, Philos. Mag. 92 (2012) 1523–1541.
[28] P. Carrez, D. Ferré, P. Cordier, Peierls-Nabarro modelling of dislocations in MgO from ambient pressure to 100 GPa, Modell. Simul. Mater. Sci. Eng. 17 (2009) 035010.
[29] P. Carrez, J. Godet, P. Cordier, Atomistic simulations of ½ < 110 > screw dislocation core in magnesium oxide, Comp. Mater. Sci. 103 (2015) 250–255.
[30] A. Hunter, R.F. Zhang, I.J. Beyerlein, The core structure of dislocations and their relationship to the material gamma-surface, J. Appl. Phys. 115 (2014).
[31] X.-Z. Wu, R. Wang, S.-F. Wang, Q.-Y. Wei, Ab initio calculations of generalized-stacking-fault energy surfaces and surface energies for FCC metals, Appl. Surf. Sci. 256 (2010) 6345–6349.
[32] G. Kresse, J. Furthmuller, Efficient iterative schemes for ab initio total-energy calculations using a plane-wave basis set, Phys. Rev. B 54 (1996) 11169–11186.
[33] G. Kresse, D. Joubert, From ultrasoft pseudopotentials to the projector augmented-wave method, Phys. Rev. B 59 (1999) 1758–1775.
[34] P.E. Blöchl, Projector augmented-wave method, Phys. Rev. B 50 (1994) 17953–17979.
[35] H.J. Monkhorst, J.D. Pack, Special points for Brillouin-zone integrations, Phys. Rev. B 13 (1976) 5188–5192.
[36] A.H. MacDonald, Comment on special points for Brillouin-zone integrations, Phys. Rev. B 18 (1978) 5897–5899.
[37] U. Schönberger, O.K. Andersen, M. Methfessel, Bonding at metal-ceramic interfaces; AB Initio density-functional calculations for Ti and Ag on MgO, Acta Metall. Mater. 40 (1992) S1–S10.
[38] J.R. Smith, T. Hong, D.J. Srolovitz, Metal-ceramic adhesion and the Harris functional, Phys. Rev. Lett. 72 (1994) 4021–4024.
[39] Y. Zhang, Y. Yao, The two-dimensional Peierls-Nabarro model for interfacial misfit dislocation networks of cubic lattice, Eur. Phys. J. B 55 (2007) 355–362.
[40] O. Nguyen, M. Ortiz, Coarse-graining and renormalization of atomistic binding relations and universal macroscopic cohesive behavior, J. Mech. Phys. Solids 50 (2002) 1727–1741.
[41] C. Qin, L.S. Sremaniak, J.L. Whitten, CO Adsorption on Ag(100) and Ag/MgO(100), J. Phys. Chem. B 110 (2006) 11272–11276.
[42] D.M. Duffy, J.H. Harding, A.M. Stoneham, Atomistic modelling of metal-oxide interfaces with image interactions, Philos. Mag. A 67 (1993) 865–882.
[43] Y.F. Zhukovskii, E.A. Kotomin, P.W.M. Jacobs, A.M. Stoneham, Ab initio modeling of metal adhesion on oxide surfaces with defects, Phys. Rev. Lett. 84 (2000) 1256–1259.
[44] C. Li, R. Wu, A.J. Freeman, C.L. Fu, Energetics, bonding mechanism, and electronic structure of metal-ceramic interfaces: Ag/MgO(001), Phys. Rev. B 48 (1993) 8317–8322.
[45] S. Plimpton, Fast parallel algorithms for short-range molecular dynamics, J. Comput. Phys. 117 (1995) 1–19.
[46] A. Stukowski, Visualization and analysis of atomistic simulation data with OVITO–the Open Visualization Tool, Modell. Simul. Mater. Sci. Eng. 18 (2010) 1–7.
[47] T. Darden, D. York, L. Pedersen, Particle mesh Ewald: An N·log(N) method for

Ewald sums in large systems, J. Chem. Phys. 98 (1993) 10089–10092.
[48] J.H. Irving, J.G. Kirkwood, The statistical mechanical theory of transport processes. IV. The equations of hydrodynamics, J. Chem. Phys. 18 (1950) 817–829.
[49] Y. Jiang, Y. Wei, J.R. Smith, J.W. Hutchinson, A.G. Evans, First principles based predictions of the toughness of a metal/oxide interface, Int. J. Mater Res. 101 (2010) 8–15.
[50] D.R.P. Singh, N. Chawla, G. Tang, Y.L. Shen, Micropillar compression of Al/SiC nanolaminates, Acta Mater. 58 (2010) 6628–6636.
[51] D. Bhattacharyya, N.A. Mara, P. Dickerson, R.G. Hoagland, A. Misra, Compressive flow behavior of Al–TiN multilayers at nanometer scale layer thickness, Acta Mater. 59 (2011) 3804–3816.
[52] W.M. Fr, D.-H. Yoon, K. Raju, S. Kim, K.-S. Song, J.H. Yu, Interfacial microstructure and shear strength of reactive air brazed oxygen transport membrane ceramic–metal alloy joints, Met. Mater. Int. 24 (2018) 157–169.
[53] X. Dai, J. Cao, J. Liu, D. Wang, J. Feng, Interfacial reaction behavior and mechanical characterization of ZrO_2/TC4 joint brazed by Ag–Cu filler metal, Mater. Sci. Eng.: A 646 (2015) 182–189.